Aggregation-induced nonlinear optical effects of AIEgen nanocrystals for ultra-deep *in vivo* bio-imaging

Zheng Zheng[1,†], Dongyu Li[2,†], Zhiyang Liu[1], Hui-Qing Peng[1], Herman H. Y. Sung[1], Ryan T. K. Kwok[1], Ian D. Williams[1], Jacky W. Y. Lam[1], Jun Qian[2,*] & Ben Zhong Tang[1,3,4,*]

[1]Department of Chemistry, Hong Kong Branch of Chinese National Engineering Research Center for Tissue Restoration and Reconstruction, Institute for Advanced Study, Department of Chemical and Biological Engineering, Institute of Molecular Functional Materials, Division of Life Science and State Key Laboratory of Molecular Neuroscience, The Hong Kong University of Science and Technology, Clear Water Bay, Kowloon, Hong Kong, China

[2]State Key Laboratory of Modern Optical Instrumentations, Centre for Optical and Electromagnetic Research, College of Optical Science and Engineering, Zhejiang University, Hangzhou 310058, China

[3]HKUST-Shenzhen Research Institute, No. 9 Yuexing 1st RD, South Area, Hi-tech Park, Nanshan, Shenzhen 518057, China

[4]Center for Aggregation-Induced Emission, SCUT-HKUST Joint Research Institute, State Key Laboratory of Luminescent Materials and Devices, South China University of Technology, Guangzhou 510640, China

[†]Zheng Zheng and Dongyu Li contributed equally to this work.

*Corresponding author: Qian Jun (qianjun@zju.edu.cn); Ben Zhong Tang (tangbenz@ust.hk)

Abstract

Nonlinear optical microscopy has become a powerful tool in bioimaging research due to its unique capabilities of deep optical sectioning, high spatial resolution imaging and three-dimensional reconstruction of biological specimens. Developing organic fluorescent probes with strong nonlinear optical effects, in particular third-harmonic generation (THG), is promising for exploiting nonlinear microscopic imaging for biomedical applications. Herein, we succesfully demonstrate a simple method for preparing organic nanocrystals based on an aggregation-induced emission (AIE) luminogen (DCCN) with bright near-infrared emission. Under femtosecond laser excitation, the high-order nonlinear optical effects of DCCN were studied in

three distinct systems, including monomolecules in solution, amorphous nanopaticles, and crystaline nanopaticles. Results revealed aggregation-induced nonlinear optical (AINLO) effects, including two-photon fluorescence (2PF), three-photon fluorescence (3PF) and THG, of DCCN in nanopaticles, especially for the crystaline nanopaticles. Taking advantage of the strong 2PF and THG properties, the nanocrystals of DCCN have been successfully applied for 2PF microscopy at 1040 nm NIR-II excitation and THG microscopy at 1560 nm NIR-II excitation, respectively, to reconstruct the 3D vasculature of the mouse cerebral vasculature. Impressively, the THG microscopy could provide much higher spatial resolution and brightness than the 2PF microscopy and could visualize small vessels with diameters of ~2.7 μm at deepest depth of 800 μm in mouse brain, which is among the largest penetration depth and best spatial resolution of *in vivo* THG vasculature imaging. Thus, this is expected to inspire new insights into development of advanced AIE materials with multiple nonlinearity, in particular THG, for multimodal nonlinear optical microscopy.

Introduction

Nonlinear optical scanning microscopy (NLOM) has drawn much attention in recent years and has been widely used in various noninvasive biological applications such as *in vitro* and *in vivo* imaging.[1-4] Especially, it has become a promising tool for brain nerve scientific research. [5-11] NLO effect is a frequency upconversion process, in which light with long wavelength is used to excite the signal light with short wavelength. Thus, NLOM will be able to translate the excitation wavelengh from visible light to first near-infrared (NIR-I, 700-900 nm) even to second near infrared (NIR-II, 900-1700 nm) window with much less scattering to provide superior optical penetration and better optical focusing in biological tissues.[12] Thus, the imaging depth of NLOM could be very large. In addition, due to the nonlinear dependence on the excitation intensity, the generated signal has a small confinement when the excitation light is concentrated.[13] Such feature endows NLOM a intrinsic high signal-to-background ratio (SBR) and sectioning capability without a confocal pinhole. Moreover, the spatial localization of nonlinear process within NLOM leads to less tissue damage to the regions above and below the focal plane that are not being imaged.[14] Due to the significant advantages mentioned above, NLOM could provide a clear vision of vasculature,[15-17] fiber texture[18,19] and neural activity in the deep region of cerebral cortex,[20] and has been utilized in specific disease research[21,22] and behavior understanding.[23]

To meet the various requirements of NLOM, a large number of organic fluorophores have been rationally designed and synthesized.[24-28] Generally, the NLO property of organic fluorophores can be achieved by fabrication of strong dipolar and long π-conjugated donor-acceptor (D-A) structures.[26] Moreover, the NLO property can also be efficiently improved by exploiting intermolecular interactions.[29-31] Hu et al. recently demonstated that intermolecular charge-transfer interactions can greatly facilitate two-photon absorption in styrylpyridine-tetracyanobenzene cocrystallization.[32] Although strong D-A strength and/or large rigid π-extended structure could endow fluorophores with interesting NLO properties, these features also make them prone to aggregate in physiological environment where their emission is often weakened or even completely quenched mainly due to the strong intermolecular dipole–dipole or π-π interactions.[33] Such a problem of aggregation-caused quenching effect has been solved by the discovery of a phenomenon of aggregation-induced emission (AIE) in 2001.[34] AIE is exact opposite of ACQ and its mechanism is closely related to the restriction of intramolecular motion in different molecular states. Typically, the formation of aggregates serves as an effective way to rigidify the structure and restrict the intramolecular motion to trigger strong light emission of the molecules.[35-37] AIE luminogens (AIEgens) therefore serve as good alternatives to conventional fluorophores and show huge potential for NLOM for their high brightness and markedly increased photostability in the aggregate state.[38-42] Generally, to improve the biocompatibility and colloidal stability, the AIEgens are often made into nanoparticles (NPs) via nanoprecipitation method by quick injection of the AIEgen solutions into aqueous media.[36,43] This rapid precipitation process would not be able to allow molecules arrange in an ordered way and often yields amorphous NPs with disordered molecules in a loose packing way. The loose packing in NPs allows efficient intramolecular motions to enable the consumption of the excited-state energy through nonradiative relaxation pathways to decrease the brightness of AIE NPs.[44-46] On the other hand, crystalization is an effective approach to maximize the packing of molecules and minimizes intramolecular motions. It is an effective way to increase the brightness of many AIEgens.[47-55] However, the preparation of crystals with sizes suitable for biological imaging is tricky. Liu et al. reported a stress-induced seed assisted crystallization method, which can produce uniform AIE nanocrystals with sizes of around 100 nm.[56] These nanocrystals show bright greenish-yellow emission and can be applied for biological imaging. Despite few atempts have been reported, developing a simple strategy to reduce the size of crystals of AIEgens is still

much sought after for NLOM. If these AIEgens exhibit also bright NIR emission, they gain additional advantages for signal collection in terms of penetration depth and spatial resolution.[57]

Two-photon fluorescence (2PF) imaging[58-66] is an effective approach to realize deep-tissue and high-resolution bioimaging, both of which can be further improved through three-photon fluorescence (3PF) imaging[67-70] and third-harmonic generation (THG)[71,72]. It is because the intensity of 3PF and THG is proportional to the cube of the excitation light power while the intensity of 2PF is proportional to the square of the excitation light power. Thus, in 3PF and THG microscopy, the three-photon excitation occurs more strongly within a spatially confined volume at the focal plane to dramatically show improved the signal-to-background ratio (SBR) than that of 2PF microscopy. These characteristics endow 3PF and THG imaging with higher spatial resolution, better sectioning ability and lower autofluorescence than 2PF. Despite the same power dependence, THG is a third-order nonlinear optical phenomenon but 3PF belongs to a fifth-order nonlinear optical process. This suggests a much lower excitation threshold of THG than that of 3PF. These features make THG imaging a promising method for deep-tissue and high-resolution bioimaging. THG microscopy enables the observation of the interface of two materials with different refractive indexes to provide convenient mapping of innate heterogeneities in biological samples.[10,73-75] However, label-free THG imaging generally lacks selectivity to the target of interest.[75] Therefore, exogenous harmonic generation agents with strong THG are needed to enhance the imaging contrast and labeling specificity. Previous THG agents are mainly inorganic systems, such as $LiNbO_3$ crystals,[76] quantum dots,[77] gold nanoparticles[78,79], indium tin oxide nanoparticles,[80] silicon nanoparticles,[81] metal−organic frameworks,[82] two-dimensional perovskites,[83] etc. However, their biomedical applications were hindered by their low biocompatibility and biosafety. Alternatively, organic THG agents represent a ideal choice but are rarely developed. Zheng et al. reported an organized aggregate of porphyrins within lipidic nanoparticles displaying structure-associated SHG and superradiant THG and successfully used for harmonic microscopic imaging of living cells with significantly enhanced contrast.[84] Recently, we found that amorphous AIE nanoparticles not only showed multi-photon fluorescence but also displayed weak THG under laser irradiation. Such characteristics allowed them to be applied in superficial mice vascular imaging but the obtained results still had much room for improvement in terms of imaging depth and resolution.[17] Therefore, the development of pure organic AIEgens with strong THG for ultra-deep *in vivo* bio-

imaging is therefore of intense interest and represents a promising emerging field of research. This is also the main subject of this article.

In this contribution, we revealed for the first time the successful application of nanocrystals of an AIEgen called DCCN with AINLO effect for ultra-deep THG microscopy (up to 800 μm) in living mice. DCCN was rationally designed by attaching electron-donating diphenylamine and electron-withdrawing dicyanomethylene-benzopyran unit at the 2,7-positions of the electron-rich carbazole ring, respectively. DCCN exhibites the crystalization-induced emission (CIE) characteristic and emit in the NIR region. The formation of DCCN crystals in mixture solvent was studied by adjusting the solvent to anti-solvent ratio and the storage time and the size of the formed crystals can be well tuned to nanoscale, suitable for biological applications. Noteworthily, besides 2PF and 3PF, DCCN showed greatly boosted THG in the crystaline nanopartilces. Compared to 2PF and 3PF microscopy, THG microscopy using nanocrystals of DCCN enables ultra-deep imaging (up to 800 μm) of the mouse cerebral vasculature with much higher spatial resolution and brightness, giving rise to a vivid 3D reconstruction of the cortical vasculature.

Results

Synthesis and photophysical property. The synthetic route of DCCN was shown in Supplementary Scheme S1 and Fig. 1A. The key step in the synthesis of DCCN was the Knoevenagel condensation of 7-(diphenylamino)-9-ethyl-9H-carbazole-2-carbaldehyde with 2-(2-methyl-4H-chromen-4-ylidene)malononitrile in reflux toluene. DCCN and the intermediates were subsequently characterized by ^{1}H NMR, ^{13}C NMR and high resolution mass spectroscopies and X-ray crystallography with satisfactory results corresponding to their molecular structures (Supplementary Fig. S1-S5). Prior to the optical study of DCCN, density functional theory (DFT) calculation was performed (Fig. 1B). The electron clouds of the HOMO were mainly located on the diphenylamino and carbazole units, whereas the orbitals of LUMO were primarily localized on the acceptor moiety. The band gap was calculated to be 2.38 eV. This suggested an intramolecular charge transfer (ICT) characteristic of the molecules.

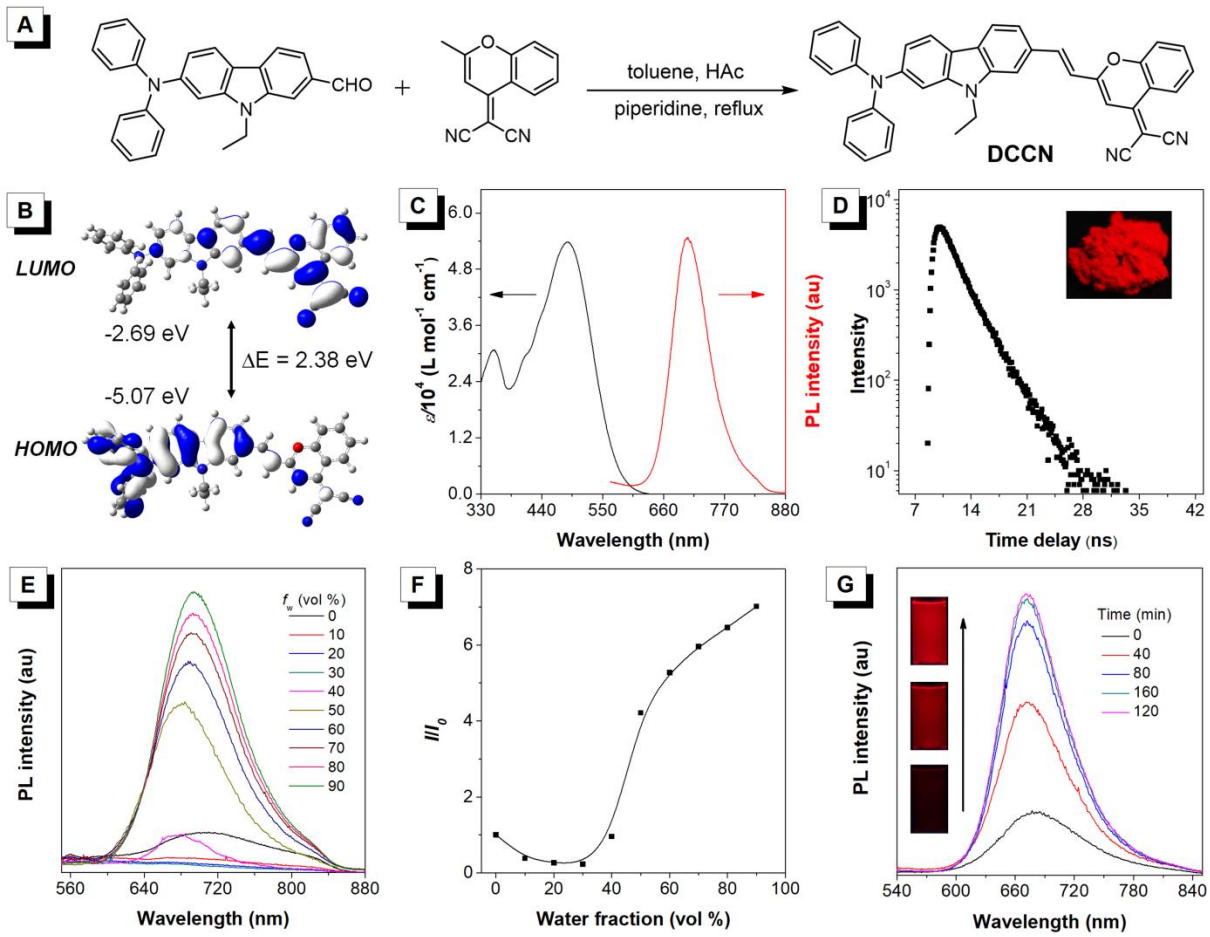

Fig. 1 (A) Synthetic route to DCCN. (B) Molecular orbital amplitude plots of HOMO and LUMO of DCCN calculated at the B3LYP/6-31G based on the single-crystal structure. (C) Absorption spectrum of DCCN in DMSO (black) and photoluminescence (PL) spectrum of DCCN in the solid state (red). (D) Fluorescence decay curve of DCCN in the solid state. Inset: fluorescent photograph of powder of DCCN taken under UV irradiation. (E) PL spectra of DCCN in acetone/water mixtures with different water fractions. [DCCN] = 10 μM. (F) Plot of relative PL intensity (I/I_0) vs the composition of the acetone/water mixtures of DCCN. (G) Time-resolved PL spectra of DCCN in acetone/water mixture (10 μM) with 50% water fraction. Inset: fluorescent photographs of the suspensions taken under UV irradiation. Excitation wavelength: 480 nm.

The absorption spectrum of DCCN in acetone (Fig. 1C) was peaked at 487 nm due to ICT from the electron-donating diphenylamino group to the electron-accepting group. The solvent effect on its optical property was then studied (Supplementary Fig. S6). The absorption of DCCN was slightly affected by the solvent polarity but a remarkable positive solvatochromism on its photoluminescence (PL) was observed. The PL maximum shifted gradually from λ_{em} = 553 to 722 nm with increasing the solvent polarity from hexane to dichloromethane. However, the PL of DCCN was greatly weakened or even quenched in polar solvent such as dimethylsulfoxide. This suggested a strong twisted intramolecular charge transfer (TICT) effect in polar media.

Impressively, DCCN exhibited a bright NIR emission centered at 704 nm in the solid state. Its fluorescence quantum yield was determined to be 12% by integrating sphere (Fig. 1C) and time-resolved fluorescence measurement in the solid state revealed a lifetime of 2.44 ns (Fig. 1D). The AIE characteristic of DCCN was evaluated in acetone/water mixtures with different water fractions (f_w). As shown in Fig. 1E and 1F, DCCN displayed a weak PL in pure acetone solution. When the water fraction was gradually increased from 0 to 30 %, the PL decreased due to the enhancement of the TICT effect resulted from the increase in the solvent polarity upon water addition. The PL strengthened again when the f_w was further increased from 40 to 90%. At 90% water fraction, the PL intensity was 7.0-fold higher than that in pure acetone, revealing the AIE property of DCCN. The emission enhancement was attributed to the formation of the nanoaggregates, which restricted the intramolecular motion to trigger the AIE effect and enhance the PL of the molecule. The observation of decreased and broadened absorption spectra of DCCN in acetone/water mixtures with high f_w also suggested the formation of nanoscopic aggregates (Supplementary Fig. S7). The absorption and PL maximum in 90% aqueous solution were 509 and 694 nm, respectively, giving rise to a large Stokes shift of 185 nm that are favorable for bio-imaging due to the minimized interference between excitation and emission.

Crystallization and crystallization-induced emission. Interestingly, the PL of a freshly prepared suspension with f_w = 50% changed constantly when standing at room temperature with time. As shown in Fig. 1G, the PL spectrum has progressively intensified and its width became narrower as time elapsed. A 4.5-fold enhancement in emission intensity was observed in 2 h. The PL maximum also gradually blue shifted from 681 to 671 nm. Such observations were consistent with the characteristics of CIE behavior and were commonly observed in AIE luminogens with blue to yellow emission.[47-54,56] For better understanding this phenomenon, the morphology evolution of aggregates formed in 50% aqueous solution was studied at different time intervals during storage. The scanning electron microscopic (SEM) image of nanoaggregates of the as-prepared suspension revealed spherical morphology as a result of quick precipitation (Fig. 2A). However, long fibers started to appear in 50% aqueous solution in 2 min (Fig. 2B). After 10 min, the spherical nanoaggregates were completely transformed into fibers (Fig. 2C). As time went by, the long fibers started to transform into thin micro rods in 20 min and eventually formed micro block morphology after 5 h (Fig. 2D-2G). A similar morphology evolution of aggregates was also found for suspensions with f_w = 60, 70 and 80%, respectively, but not for suspensions with

higher f_w values (Supplementary Fig. S8). Apparently, with increasing f_w of the suspension, the time of this evolution process was significantly prolonged. Finally, crystals with different sizes of 3.58 μm, 2.32 μm, 401 nm and 129 nm were obtained for suspensions with f_w = 50, 60, 70 and 80%, respectively (Supplementary Fig. S9). The crystalline characteristics of the nanocrystals were further verified by X-ray diffraction (XRD) (Fig. 2K). These results demonstrated that DCCN was not only AIE but also CIE-active with NIR emission and such cases were rarely reported. Additionally, with an increase of f_w and extension of storage time, the size of the formed crystals can be facilely reduced to promising nanoscale range for biological applications. Such simple protocol to prepare nanocrystals was also believed applicable to other organic molecules with AIE or CIE properties.

Crystal structure. The CIE effect and strong solid-state fluorescence of DCCN encourage us to further study its molecular conformation and molecular packing in the crystalline state. The single crystals of DCCN suitable for X-ray crystallography were obtained by slow evaporation from its ethanol/CH_2Cl_2 mixture. The crystal data and the collection parameters were summarized in Supplementary Table S1 (CCDC 1939907). DCCN crystallized in the monoclinic $P2_1/c$ space group with an elemental cell containing four molecules. Single crystal X-ray diffraction analyses provided direct evidence for the *trans*-conformation of DCCN. In the crystal structure, the small dihedral angle of 3.07 ° between the 2-(4H-chromen-4-ylidene)malononitrile and carbazole moieties suggested that they were essentially planar and conjugated, both of which allowed good π-electron delocalization over the whole molecule (Fig. 2L). Thus, the strong push-pull character together with the extended *π*-conjugation within the fluorophore effectively resulted in NIR emission. It was clearly found that an antiparallel dimer was formed along the long molecular axis through close intermolecular π-π interaction with a slip angle of 33.78 ° and a short distance of 3.37 Å (Fig. 2M, Supplementary Fig. S10A). Furthermore, each dimeric molecule experienced two same intermolecular π-π interactions (3.39 Å) between the carbazole and the 2-(4H-chromen-4-ylidene)malononitrile units with two adjacent molecules. It was noted that the distances of the intermolecular π–π interactions were shorter than the typical values (3.5 Å). In the crystalline state, these short intermolecular π-π interactions together with multiple intermolecular C-H···π and C≡N ··H interactions rigidified the molecular conformation and restricted the intramolecular motions in a greater extent than in the amorphous state. Thus, the excited-state energy consumed by intramolecular motions was greatly reduced to enable the

molecules to emit stronger NIR emission in crystals. On the other hand, the cooperation of various interactions in particular the close π–π stacking directed the DCCN molecules to self-assemble into a brickwork arrangement within the crystal bc plane, in which "J-type" coupling was preferred (Fig. 2M and Fig. 2N). It was clearly observed that there existed infinite continuous intermolecular π–π interactions with alternant intermolecular D–A effect among the molecular packing structures (Supplementary Fig. S10B), which enabled the intermolecular electron coupling in the crystal packing structure.

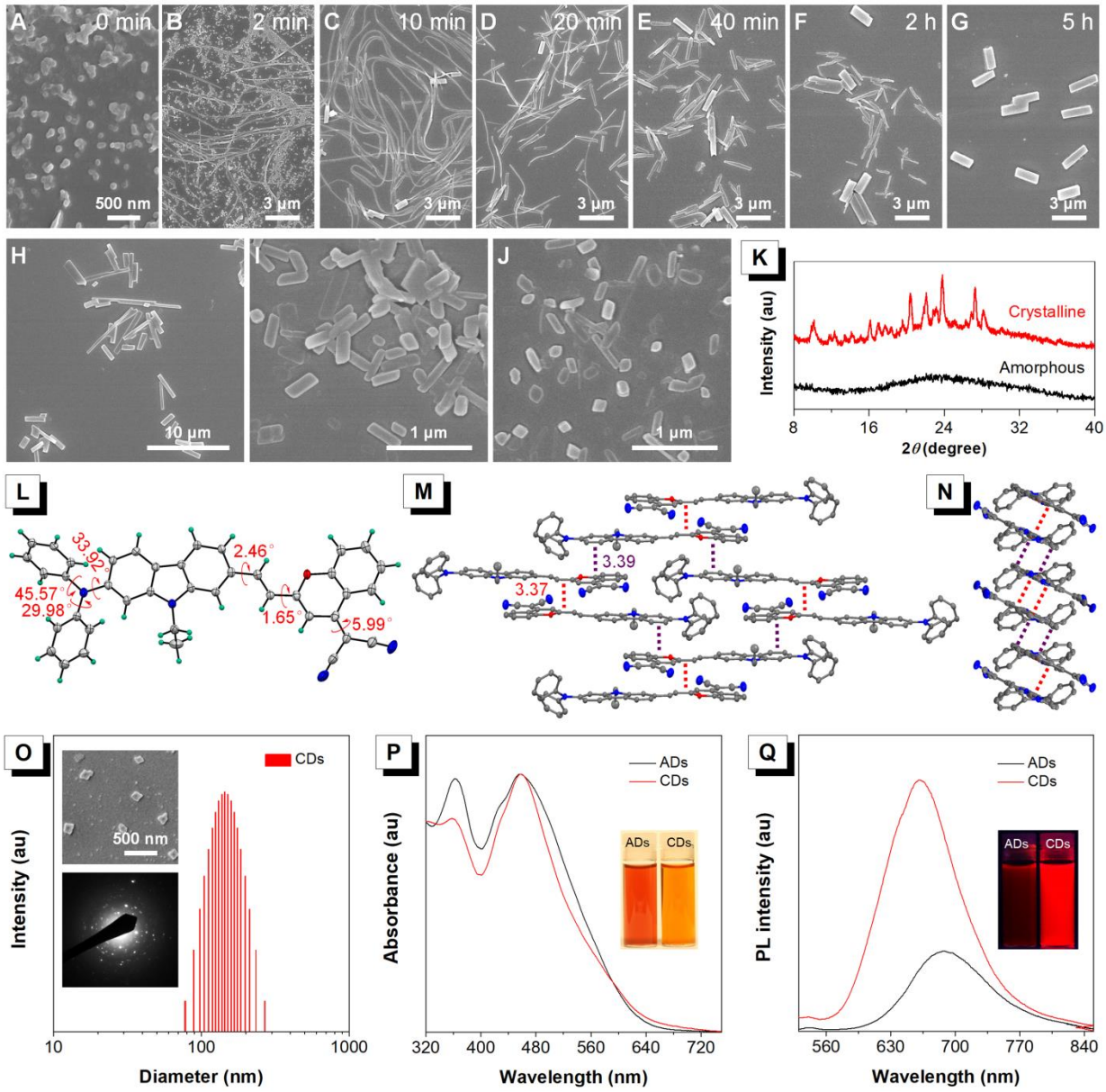

Fig. 2 SEM images of DCCN in a acetone/water mixture with water fraction (f_w) of 50% taken at different storage time: (A) 0 min, (B) 2 min, (C) 10 min, (D) 20 min, (E) 40 min, (F) 2 h and (G) 5 h. SEM images of DCCN nanoparticles formed in acetone/water mixtures with water fractions of (H) 60%, (I) 70%, and (J) 80%. (K) XRD

patterns of DCCN nanoaggregates before and after crystallization in an acetone/water mixture with f_w = 80%. (L) Single-crystal structure of DCCN and molecular π–π stacking structures along (M) the long molecule axis and (N) the short molecule axis. (O) Hydrodynamic mean particle size distribution of crystalline dots (CDs) by dynamic light scattering along with their SEM image and SAED pattern. (P) Absorption and (Q) PL spectra of DCCN in amorphous dots (ADs) and CDs in water. Excitation wavelength: 480 nm. The insets of (P) and (Q) showed the fluorescent photographs of the suspensions taken under daylight and UV irradiation, respectively.

Preparation of amorphous dots and crystalline dots. To improve their colloidal stability and biocompatibility in physiological conditions, the nanocrystals obtained from 80% aqueous solution were encapsulated by Pluronic F127 matrix, yielding crystalline dots (CDs) with a slightly increased size of 143 nm (Fig. 2O and Supplementary Fig. S11). The morphology and crystalline feature of CDs were well characterized by SEM and the selected-area electron diffraction pattern (SAED). For better comparison, amorphous dots (ADs) were also prepared by encapsulating DCCN in Pluronic F127 matrix via a nanoprecipitation method (Supplementary Fig. S12). As illustrated in Fig. 2P, the absorption spectrum of CDs displayed slight difference from that of ADs, both showing an absorption maximum at ~458 nm. Significantly, the PL of CDs was stronger than that of ADs by more than 320% accompanied with a blue-shift in the emission maximum by 28 nm (Fig. 2Q and Supplementary Fig. S13). These results demonstrated the boosted emission property of CDs over ADs taking advantage of their regular and close molecular packing.

Aggregation-induced nonlinear optical effect. Owing to the strong push–pull dipolar character and the extended π-conjugation of DCCN, interesting nonlinear optical properties, such as 2PF, 3PF and THG, can be expected for its CDs (Fig. 3A). The nonlinear optical response of CDs was studied on a lab-built nonlinear optical spectral measurement system (Supplementary Fig. S14). Under the excitation of a 1040 nm fs laser, the fluorescence spectrum of CDs was recorded (Fig. 3B). The logarithm of the fluorescence intensity of CDs and the logarithm of the excitation power were found to have a good linear relationship with a calculated slope of 1.81 (very close to 2), indicative of 2PF nonlinear optical process (Supplementary Fig. S15A). In this two-photon excitation process, the fluorophore simultaneously absorbed two photons of 1040 nm and was pumped to the excited state, which further underwent radiative decay to release a photon (Fig. 3A). In addition to 2PF, impressive 3PF and in particular THG signals of CDs were observed under the excitation of a 1560 nm fs laser, which was close to thrice the wavelength of absorption maximum (Fig. 3C). Different from the two-photon process, three photons of 1560

nm were absorbed simultaneously in the three-photon excitation process, followed by the same radiative decay pathway as those of one and two-photon processes as suggested by their similar PL spectra (Fig. 3A). Accordingly, the power dependence relationship of the fluorescence of CDs was studied by plotting the logarithm of 3PF intensity of CDs and the logarithm of the excitation power. The resulting curve showed a very good linear relationship and the slope was calculated to be 2.86 (close to 3), confirming a three-photon absorption process (Supplementary Fig. S15B). In addition to 3PF, it was surprising to simultaneously observe strong THG signal peaked at ~520 nm under the same excitation of a 1560 nm fs laser. With increasing the power of the excitation source, an exponential increase in the generated signal with a power of 2.69 (close to 3) was observed. This implied that the signal collected was attributed to the third-order optical nonlinearity (Supplementary Fig. S15C). Now, it was realized that the crystalline nanoparticles of DCCN exhibited novel NLO properties. How about its isolated species in pure solution and ADs? As shown in Supplementary Fig. S16, the ADs of DCCN also showed 2PF, 3PF and THG properties. Fig. 3D shows the photographs of the capillaries containing DCCN solution, ADs and CDs. Under the same excitation of 1040 nm (for 2PF) and 1560 nm (for 3PF) fs laser, the DCCN solution displayed very weak 2PF and 3PF. The ADs showed stronger 2PF and 3PF, being 1.9 and 1.5-fold higher than those values in the solution. Such enhancement effect might be attributed to the AIE characteristic of DCCN. Interestingly, CDs exhibited enhanced 2PF and 3PF intensities than those of solution by 7.6- and 2.4-fold respectively, mainly due to the CIE effect of DCCN. On the other hand, at the same excitation of a 1560 nm fs laser, almost no THG signal was recorded from the solution but a 366-fold higher signal was detected in ADs, which could be attributed to the intrinsic third-order nonlinear optical susceptibility of DCCN together with the generated interface between aqueous medium and nanoparticles. Impressively, the THG intensity was boosted by 1183-fold from the solution state to CDs. The much stronger THG of CDs than ADs was believed to be attributed to the extensive electron coupling within its unique brickwork molecular arrangement in the crystalline state, which was also demonstrated to amplify the third-order nonlinear property of D–A type oligo-phenylene vinylenes.[85] These results clearly demonstrated aggregation-induced 2PF, aggregation-induced 3PF and aggregation-induced THG effects in ADs. These effects were further strength in CDs due to the stronger RIM effect. All these effects can be integrated as aggregation-induced nonlinear optical (AINLO) effect.

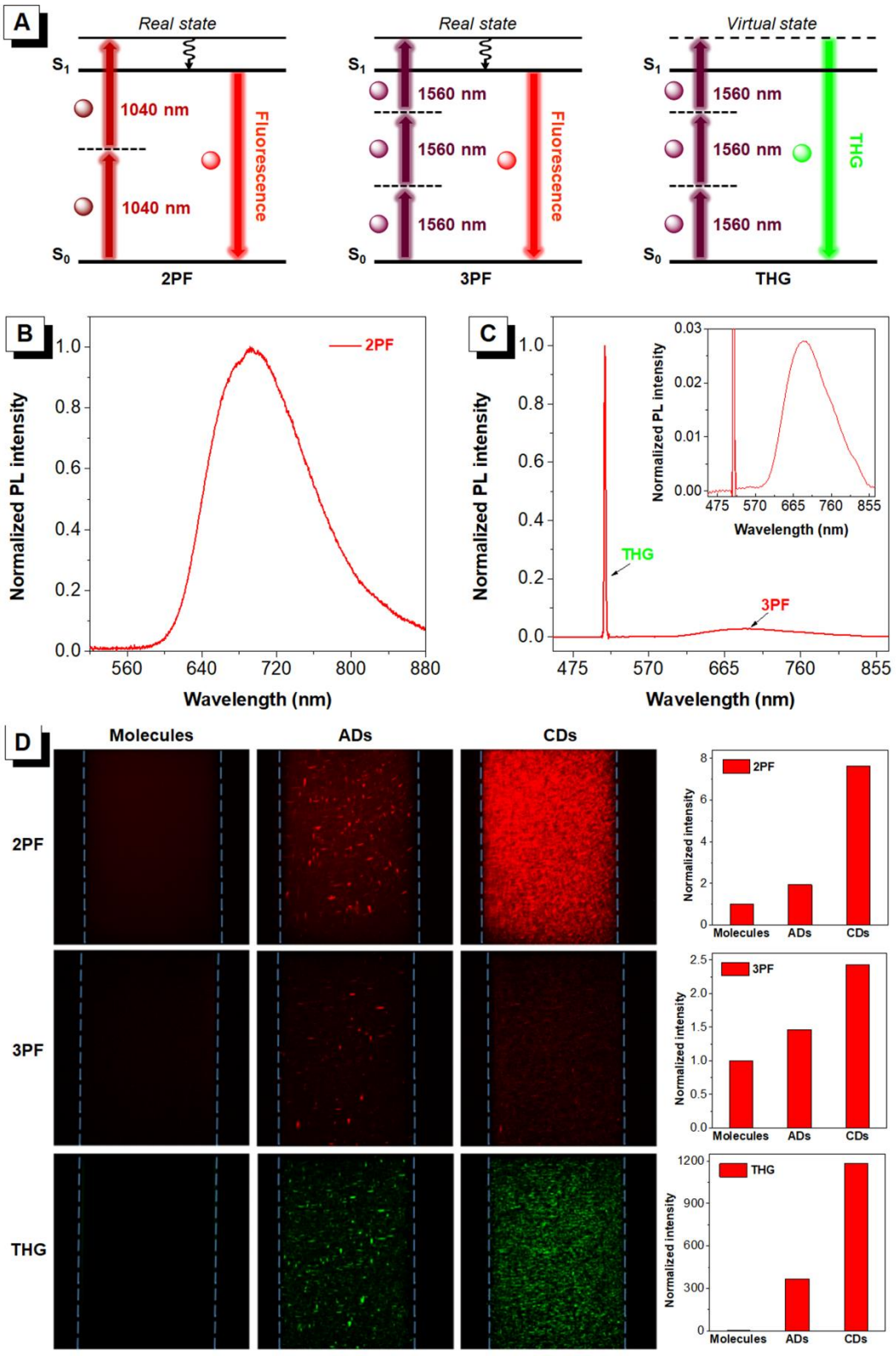

Fig. 3 (A) Schematic illustration of 2PF, 3PF and THG processes. (B) 2PF spectrum of CDs in water. (C) 3PF and THG spectra of CDs in water. Inset was the intensified spectrum at a wavelength range of 450-870 nm. (D) 2PF, 3PF and THG images of acetone solution, ADs and CDs in capillary glass tube.

Ultra-deep *in vivo* THG imaging. Considering the 3PF of CDs was not strong, THG microscopy was used for deep cortical vessel imaging and the result obtained was compared with that of 2PL microscopy (Supplementary Fig. S17). As shown in Fig. 4, the 2PF and THG scanning microscopies were carried out with the same 2D area of 500 μm × 500 μm on the mouse brain after injection of the CDs through the tail vein. At 200 μm depth, there was little difference between two imaging methods. The signal intensity and the signal-background ratio (SBR) were similar. When it came to 260 μm, there was a "Y shaped" vessel and its "shadow" was reflected on the 2PF image at 300 μm depth as indicated in the dashed circle, while the THG image at 300 μm was much clearer. Although both 2PF and THG are third-order nonlinear optical phenomenon, the intensity of THG is proportional to the cube of the excitation light intensity and the intensity of 2PF is proportional to the square of the excitation light intensity. Thus, the intensity of THG decays faster with an increase of the defocusing distance. As a consequence, the axial resolution of THG microscopy is much better than 2PF microscopy. Furthermore, when the focal depth became deeper, the excitation power should be upgraded due to the attenuation of excitation light and signal light in the tissue. This makes the laser power density became stronger at surface as well. Thus, the 2PF at surface could also be excited and then collected by the photomultiplier tube (PMT). However, since the order of the corresponding dependence of THG on excitation light power density is higher than that of 2PL, THG shows smaller confinement. As a consequence, during the deep-tissue THG imaging, the out-of-focus signals including surficial signals are less likely to be excited. As shown in Fig. 4, at 400 μm depth, the background noise of 2PF microcopy was obviously higher than THG microscopy due to the surficial signal, which hindered the clear observation of some vessels. Some vasculatures at 500 μm depth could not be observed anymore by 2PF microscopy because of the background noise from the surface but could still be distinguished using THG microscopy. Finally, the cortical vasculature could be observed with THG microscope at 710 μm depth, where only background noise could be obtained by 2PF microscopy at the same depth. Due to the shortcomings of 2PF imaging with low axial resolution and surface signal interference to deep signals, its resolution at each particular depth was not as good as THG imaging, especially at a deep position, which was clearly illustrated by the intensity profile along the indicated white line across the vasculature at each particular depth.

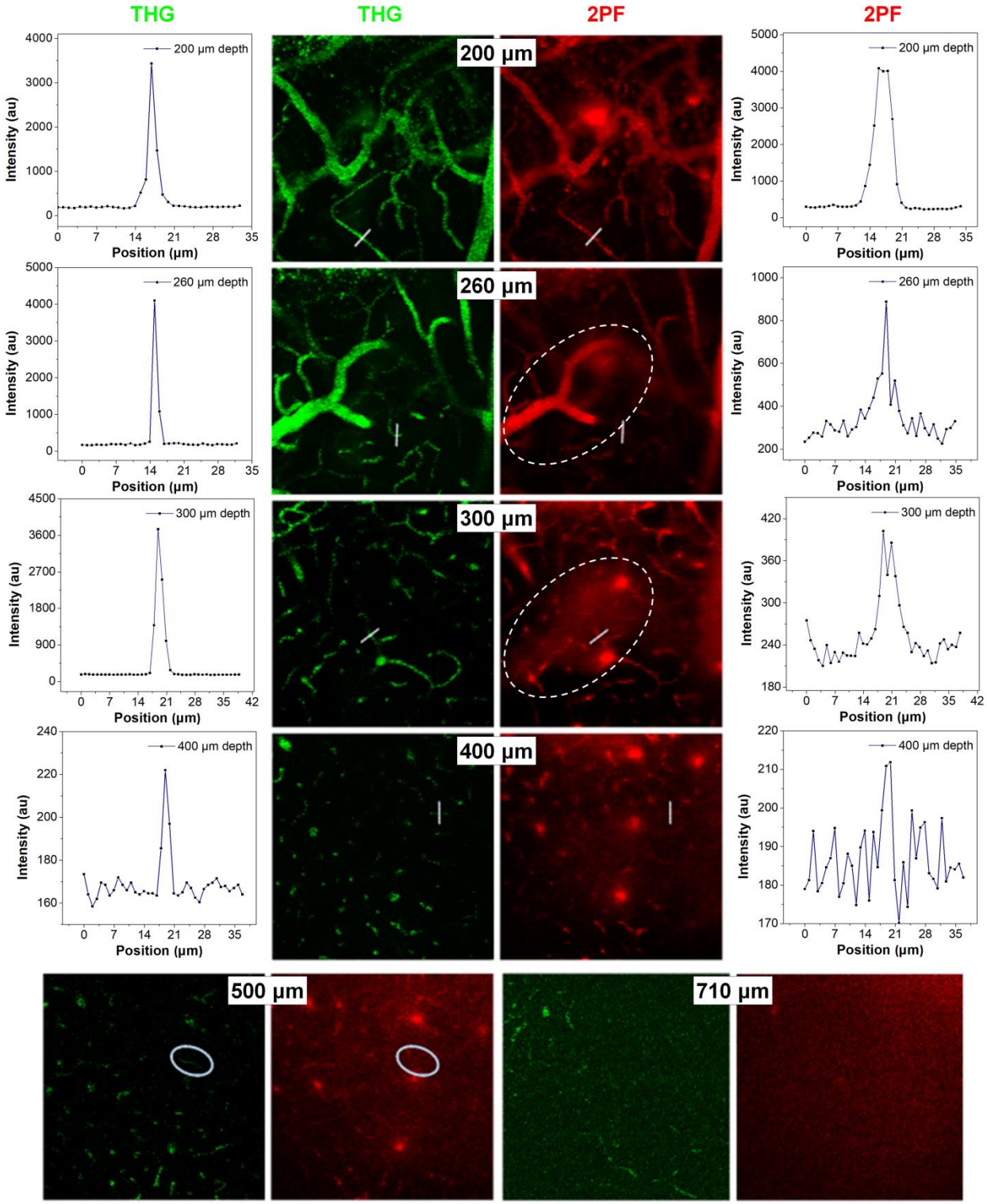

Fig. 4 Comparison of 2PF and THG microscopic imaging of cortical vasculature at different depths by using intravenously injected CDs. The 2PL and THG images were taken under the NLO microscope equipped with 1040 nm and 1560 nm fs laser. Intensity profile along the white line across the vasculature was plotted respectively.

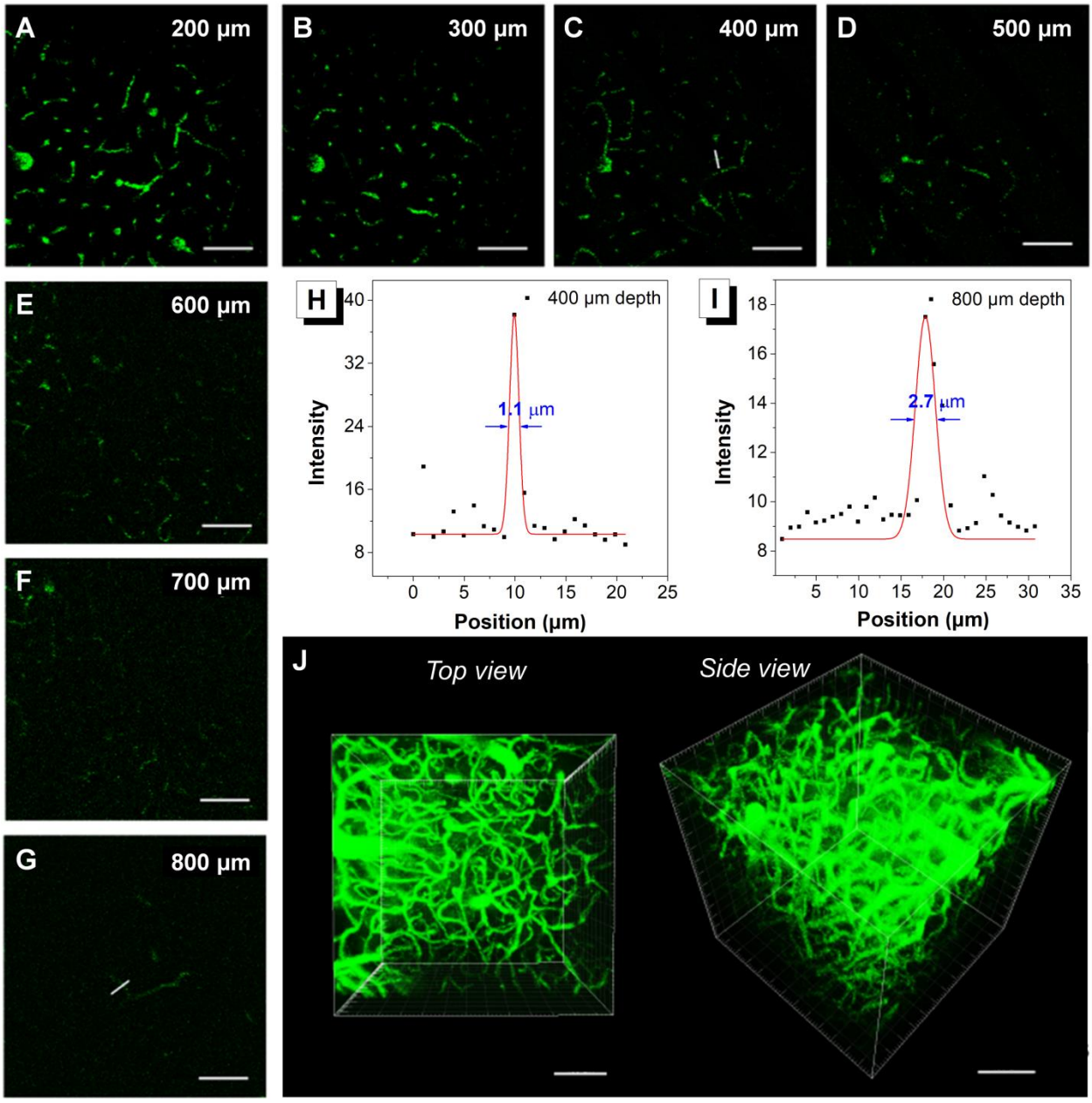

Fig. 5 (A-G) In vivo THG microscopic imaging of CDs-stained cortical vasculature at different depths as indicated. (H, I) fwhm of a blood vessel at the depth of (H) 400 μm and (I) 800 μm as indicated with the white line in (C) and (G) images. (J) Three dimensional reconstruction of the vasculature from top to 800 μm depth. The scale bars in (A-G) and (J) indicate 100 and 150 μm, respectively.

To exploit the utmost performance of CDs in THG microscopy, an area rich in small blood vessels was chosen for deep-tissue imaging. As shown in Fig. 5A-5D, the vasculature could be clearly observed with low background noise. When it came to 600 μm depth, the THG signal became weaker due to the attenuation of the excitation and THG light in tissue (Fig. 5E).

However, the vasculature could still be distinguished at deeper focal planes (Fig. 5F and 5G). To gain a better evaluation of the imaging quality, lines were drawn across tiny capillaries at depth of 400 μm, and the pixel intensity was plotted as a function of position (Fig. 5H). The Gaussian fitting provided the profile of a capillary, which afforded a full width at half-maximum (fwhm) of ~1.1 μm with high resolution. Thanks to the bright signals of CDs and good confinement, the penetration ability of THG microscopy could reach 800 μm (Fig. 3G) and a small blood vessel with a diameter of ~3 μm could still be resolved at certain depth (Fig. 3I), being one of the largest penetration depths and best spatial resolutions of *in vivo* THG imaging.[18]

In contrast, deep-tissue 2PF microscopy was performed and an imaging depth of 700 μm was obtained (Supplementary Fig. S18). Since big blood vessels were avoided in the center of this region on purpose, the occlusion effect of the upper blood vessels on the lower blood vessels was relatively smaller than in Fig. 4. However, when deep blood vessels were focused, the interference of surface signals still existed, which limited the penetration ability and the lateral resolution of 2PF microscopy.

Discussion

We developed a novel AIEgen abbreviated as DCCN by attaching electron-donating diphenylamine and electron-withdrawing dicyanomethylene-benzopyran units to the electron-rich carbazole ring at 2, 7-positions. The obtained DCCN displayed CIE property with NIR fluorescence. The formation of crystals in mixture solvent was studied and it was found that the size of the resulting crystals could be well tuned by adjusting the solvent to anti-solvent ratio and the storage time. The obtained nanocrystals with bright NIR emission was highly desirable for biological applications. Under fs laser excitation, the crystaline nanoparticles of DCCN show enhanced not only 2PF and 3PF but also THG than those of amorphous nanoparticles. The strong THG of nanocrystals enabled ultra-deep imaging of the mouse cerebral vasculature and clear visualization of small vessels of ~2.7 μm at a depth of 800 μm in mouse brain with much higher spatial resolution and brightness than 2PF and 3PF imaging. As a result, a highly resolved 3D reconstruction of the cortical vasculature was realized. This work not only demonstrated a simple protocol to prepare nanocrystals based on AIEgens with good crystallinity, but also provided an ideal AIE platform with multiple nonlinearity, in particular THG, for multimodal nonlinear optical microscopy.

Methods

Materials and characterization. All chemicals and reagents were commercially available and used as received without further purification. The solvents for chemical reactions were distilled before use. The intermediates, namely 2-(2-methyl-4H-chromen-4-ylidene)malononitrile and 7-(diphenylamino)-9-ethyl-9H-carbazole-2-carbaldehyde, were synthesized according to the reported procedures.[60,86,87] ^{1}H and ^{13}C NMR spectra were measured on a Bruker ARX 400 NMR spectrometer using $CDCl_3$ as solvents and tetramethylsilane (TMS; δ = 0 ppm) as internal reference. High-resolution mass spectra (HR-MS) were obtained on a Finnigan MAT TSQ 7000 Mass Spectrometer System operated in a MALDI-TOF mode. The UV−vis−NIR absorption spectra were performed using a PerkinElmer Lambda 365 spectrophotometer. The photoluminescence spectra were conducted on a Horiba Fluorolog-3 spectrofluorometer. Dynamic light scattering (DLS) was measured using a Zetaplus Potential Analyzer (Brookhaven Instruments Corporation, USA). Scanning electron microscopy (SEM) micrographs were collected on a field emission scanning electron microscope (FESEM, JEOL-7100F). Absolute fluorescence quantum yield was measured by a calibrated integrating sphere (Labsphere). Single crystal data was collected on a SuperNova, Dual, Cu at zero, Atlas diffractometer. The crystal was kept at 100.01(10) K during data collection. Using Olex2, the structure was solved with the Superflip structure solution program using Charge Flipping and refined with the ShelXL refinement package using Least Squares minimisation.

Synthesis of DCCN. A mixture of 2-(2-methyl-4H-chromen-4-ylidene)malononitrile (0.24 g, 1.16 mmol), 7-(diphenylamino)-9-ethyl-9H-carbazole-2-carbaldehyde (0.5 g, 1.28 mmol), glacial acetic acid (0.25 mL) and piperidine (0.5 mL) in toluene (25 mL) was refluxed and stirred overnight under nitrogen. After cooling to room temperature, the precipitates was filtered, washed with cold toluene and dried. The crude product was further purified by re-crystallization from CH_2Cl_2 and hexane, affording DCCN as a dark red solid (0.37 g, yield: 55%). ^{1}H NMR (400 MHz, $CDCl_3$), δ (ppm): 8.94 (d, J = 8.3 Hz, 1H), 8.01 (d, J = 8.1 Hz, 1H), 7.92 (d, J = 8.4 Hz, 1H), 7.83 (d, J = 15.9 Hz, 1H), 7.77-7.72 (m, 1H), 7.59-7.55 (m, 2H), 7.48-7.44 (m, 2H), 7.30-7.28 (m, 4H), 7.18-7.16 (m, 4H), 7.17 (s, 1H), 7.06-7.03 (m, 2H), 6.99 (dd, J = 8.4 Hz, 1.8 Hz, 1H), 6.93 (d, J = 15.6 Hz, 2H), 4.25 (q, J = 7.2 Hz, 2H), 1.38 (t, J = 7.2 Hz, 3H). ^{13}C NMR (100 MHz, $CDCl_3$), δ (ppm): 157.36, 152.23, 151.79, 147.39, 146.93, 141.72, 139.92, 139.76, 133.88, 130.51, 128.63, 125.24, 124.81, 123.70, 122.28, 120.83, 119.59, 118.92, 117.91, 117.35,

117.34, 116.66, 116.51, 116.36, 115.35, 107.14, 105.85, 103.25, 61.36, 36.89, 13.20. HRMS (MALDI-TOF): *m*/*z* calcd. for $C_{40}H_{28}N_4O$ $[M]^+$: 580.2263, found: 580.2307.

Crystal formation. Different amounts of water were quickly injected into pure acetone solutions of DCCN (0.2 μmol) in different vials with defined water fraction (f_w = 50% to 80%) and a final volume of 20 mL. The vials were tightly capped to prevent organic solvent evaporation, and the suspensions were left in a dark place at room temperature. The crystallization process was monitored by SEM measurement until the crystallization was completed.

Preparation of CDs. After the crystallization was completed in a suspension with f_w = 80%, 1.2 mg of Pluronic F127 was added into suspension under stirring. After 2 h stirring at room temperature, the suspension was concentrated, giving a final suspension with a concentration of 1 mg mL^{-1} in terms of DCCN.

Preparation of ADs. 1 mg of DCCN and 2 mg of Pluronic F127 were dissolved in 1 mL of THF, and the solution was then quickly injected into 10 mL of water under stirring. The mixture was stirred at room temperature overnight to evaporate the organic solvent. The suspension was concentrated, giving a final suspension with a concentration of 1 mg mL^{-1} in terms of DCCN.

Nonlinear optical measurement. As shown in Supplementary Fig. S14, the fs laser (1040 nm or 1560 nm) was focused on a cuvette containing the dispersion of CDs via a lens (focal length: 5 cm). The nonlinear optical signals were collected from the laser-incident direction by an objective (XLPLN25XWMP2, Olympus, 25 × 1.05 NA) and recorded with an optical fiber spectrometer (PG 2000, Ideaoptics Instruments) after passing through a 950-nm short-pass filter.

Nonlinear optical microscopic system. Two femtosecond (fs) laser beams were induced into a commercial scanning microscope (FV1200，Olympus) as the excitation source. One of them was a 1040-nm fs laser (150 fs, 50 MHz), which was used to excite two-photon luminescence (2PL). The other one was a 1560-nm fs laser (400 fs, 1 MHz), which was used to excite third harmonic generation (THG) and three-photon luminescence (3PL). As showed in Supplementary Fig. S17, the laser beam was scanned by two computer-driven galvanometers and then reflected by a gold mirror. After passing through a scan lens and a tube lens, the laser beam was reflected by a dichroic mirror (DM1: 1,000–1,600 nm reflection, 400–950 nm transmission, customized by Chroma Technology Corp), and finally focused onto the sample by a water-immersed

microscope objective (XLPLN25XWMP2, Olympus, 25 × 1.05 NA). The excited nonlinear optical signals were epi-collected with the same objective. The signals were then passed through DM1 and were spitted by a dichroic mirror (DM2: 579 nm short pass, FV10MP-MG/R). The green channel passed through a band pass filter (495 nm-540 nm) and then was collected by a photo multiplier tube (PMT, HPM-100-50，Becher & Hickl GmbH) for THG imaging. The red channel was directly collected by a PMT (HPM-100-50，Becher & Hickl GmbH) for 2PL and 3PL imaging. D_2O instead of H_2O was used to immerse the objective when 3PL and THG imaging were conducted in order to reduce the attenuation of the 1560 nm light.

Power dependence measurement. The DCCN molecules in acetone solution, the dispersion of CDs or the dispersion of ADs was placed in the glass capillary and imaged with the nonlinear optical microscopic system working on 2PL, 3PL and THG modes. During each imaging process, the average power of the excitation beam was adjusted, and the images related to every particular excitation power were recorded. Finally, the intensity of the nonlinear optical signals was analyzed together with the related power of the excitation beam.

Animal treatments: Female ICR mice (8 weeks old) were used for all experiments. The mice were anesthetized, and their scalps and skulls were removed to carefully offer a cranial window. After that, a round thin cover glass slide was fixed onto the dura of each mouse through dental cement to protect the brain, as well as offer a cranial window. Then, the mouse was immobilized using a lab-built plate and put under the nonlinear optical microscopic system for imaging. Before imaging, the CDs dispersion in PBS (200 μL, 1 mg/mL) were injected into the mice through the tail vein. The images were taken every 5 μm, and the scanning speed of was 20 μs/pixel (512 × 512 pixels per frame).

Data availability

The authors declare that all data supporting the findings of this study are available within the article and its Supplementary Information Files.

Reference

1. Denk, W., Strickler, J.H. & Webb, W.W. Two-photon laser scanning fluorescence microscopy. *Science* **248**, 73-76 (1990).

2. König, K. Multiphoton microscopy in life sciences. *J. Microsc.* **200**, 83-104 (2000).

3. Zipfel, W.R.*, et al.* Live tissue intrinsic emission microscopy using multiphoton-excited native fluorescence and second harmonic generation. *Proc. Natl. Acad. Sci. USA.* **100**, 7075-7080 (2003).

4. Helmchen, F. & Denk, W. Deep tissue two-photon microscopy. *Nat. Methods* **2**, 932 (2005).

5. Friedl, P., Wolf, K., Harms, G. & von Andrian, U.H. Biological second and third harmonic generation microscopy. *Curr. Protoc. Cell Biol.* **34**, 4.15. 11-14.15. 21 (2007).

6. Kleinfeld, D., Mitra, P.P., Helmchen, F. & Denk, W. Fluctuations and stimulus-induced changes in blood flow observed in individual capillaries in layers 2 through 4 of rat neocortex. *Proc. Natl. Acad. Sci. USA.* **95**, 15741-15746 (1998).

7. Theer, P., Hasan, M.T. & Denk, W. Two-photon imaging to a depth of 1000 μm in living brains by use of a Ti: Al 2 O 3 regenerative amplifier. *Opt. Lett.* **28**, 1022-1024 (2003).

8. Kobat, D.*, et al.* Deep tissue multiphoton microscopy using longer wavelength excitation. *Opt. Express* **17**, 13354-13364 (2009).

9. Sun, C.-K.*, et al.* Higher harmonic generation microscopy for developmental biology. *J. Struct. Biol.* **147**, 19-30 (2004).

10. Débarre, D.*, et al.* Imaging lipid bodies in cells and tissues using third-harmonic generation microscopy. *Nat. Methods* **3**, 47 (2006).

11. Diaspro, A.*, et al.* Multi-photon excitation microscopy. *Biomed. Eng. Online* **5**, 36 (2006).

12. Xu, C., Zipfel, W., Shear, J.B., Williams, R.M. & Webb, W.W. Multiphoton fluorescence excitation: new spectral windows for biological nonlinear microscopy. *Proc. Natl. Acad. Sci. USA.* **93**, 10763-10768 (1996).

13. Zipfel, W.R., Williams, R.M. & Webb, W.W. Nonlinear magic: multiphoton microscopy in the biosciences. *Nat. Biotechnol.* **21**, 1369 (2003).

14. So, P.T., Dong, C.Y., Masters, B.R. & Berland, K.M. Two-photon excitation fluorescence microscopy. *Annu. Rev. Biomed. Eng.* **2**, 399-429 (2000).

15. Wang, S.*, et al.* Three-photon luminescence of gold nanorods and its applications for high contrast tissue and deep in vivo brain imaging. *Theranostics* **5**, 251-266 (2015).

16. Zhang, H.*, et al.* Biocompatible aggregation-induced emission nanoparticles with red emission for in vivo three-photon brain vascular imaging. *J. Mater. Chem. B* **5**, 2757-2762 (2017).

17. Wang, Y.*, et al.* Bright AIE nanoparticles with F127 encapsulation for deep-tissue three-

photon intravital brain angiography. *Adv. Healthcare Mater.* **6**, 1700685 (2017).

18. Horton, N.G.*, et al.* In vivo three-photon microscopy of subcortical structures within an intact mouse brain. *Nat. Photonics* **7**, 205 (2013).

19. Wang, T.*, et al.* Three-photon imaging of mouse brain structure and function through the intact skull. *Nat. Methods* **15**, 789 (2018).

20. Prevedel, R.*, et al.* Fast volumetric calcium imaging across multiple cortical layers using sculpted light. *Nat. Methods* **13**, 1021 (2016).

21. Iliff, J.J.*, et al.* A paravascular pathway facilitates CSF flow through the brain parenchyma and the clearance of interstitial solutes, including amyloid β. *Sci. Transl. Med.* **4**, 147ra111-147ra111 (2012).

22. Busche, M.A.*, et al.* Clusters of hyperactive neurons near amyloid plaques in a mouse model of Alzheimer's disease. *Science* **321**, 1686-1689 (2008).

23. Kain, J.*, et al.* Leg-tracking and automated behavioural classification in Drosophila. *Nat. Commun.* **4**, 1910 (2013).

24. He, G.S., Tan, L.-S., Zheng, Q. & Prasad, P.N. Multiphoton absorbing materials: molecular designs, characterizations, and applications. *Chem. Rev.* **108**, 1245-1330 (2008).

25. Pawlicki, M., Collins, H.A., Denning, R.G. & Anderson, H.L. Two-photon absorption and the design of two-photon dyes. *Angew. Chem., Int. Ed.* **48**, 3244-3266 (2009).

26. Sumalekshmy, S. & Fahrni, C.J. Metal-ion-responsive fluorescent probes for two-photon excitation microscopy. *Chem. Mater.* **23**, 483-500 (2010).

27. Kim, H.M. & Cho, B.R. Small-molecule two-photon probes for bioimaging applications. *Chem. Rev.* **115**, 5014-5055 (2015).

28. Albota, M.*, et al.* Design of organic molecules with large two-photon absorption cross sections. *Science* **281**, 1653-1656 (1998).

29. Gotoh, T., Kondoh, T., Egawa, K. & Kubodera, K.-i. Exceptionally large third-order optical nonlinearity of the organic charge-transfer complex. *J. Opt. Soc. Am. B* **6**, 703-706 (1989).

30. Collini, E. Cooperative effects to enhance two-photon absorption efficiency: intra-versus inter-molecular approach. *Phys. Chem. Chem. Phys.* **14**, 3725-3736 (2012).

31. Sanyal, S., Painelli, A., Pati, S.K., Terenziani, F. & Sissa, C. Aggregates of quadrupolar dyes for two-photon absorption: the role of intermolecular interactions. *Phys. Chem. Chem. Phys.* **18**, 28198-28208 (2016).

32. Sun, L.*, et al.* Intermolecular charge-transfer interactions facilitate two-photon absorption in styrylpyridine–tetracyanobenzene cocrystals. *Angew. Chem., Int. Ed.* **56**, 7831-7835 (2017).
33. Birks, J.B. *Photophysics of aromatic molecules*. (1970).
34. Luo, J.*, et al.* Aggregation-induced emission of 1-methyl-1, 2, 3, 4, 5-pentaphenylsilole. *Chem. Commun.*, 1740-1741 (2001).
35. Zhang, X.*, et al.* Aggregation induced emission-based fluorescent nanoparticles: fabrication methodologies and biomedical applications. *J. Mater. Chem. B* **2**, 4398-4414 (2014).
36. Yan, L., Zhang, Y., Xu, B. & Tian, W. Fluorescent nanoparticles based on AIE fluorogens for bioimaging. *Nanoscale* **8**, 2471-2487 (2016).
37. Chen, S., Wang, H., Hong, Y. & Tang, B.Z. Fabrication of fluorescent nanoparticles based on AIE luminogens (AIE dots) and their applications in bioimaging. *Mater. Horiz.* **3**, 283-293 (2016).
38. Lou, X., Zhao, Z. & Tang, B.Z. Organic dots based on AIEgens for two-photon fluorescence bioimaging. *Small* **12**, 6430-6450 (2016).
39. Wang, D. & Qian, J. AIE Luminogens for three-photon fluorescence bioimaging. in *Principles and Applications of Aggregation-Induced Emission* 425-455 (Springer, 2019).
40. Qian, J.*, et al.* High-order non-linear optical effects in organic luminogens with aggregation-induced emission. *Adv. Mater.* **27**, 2332-2339 (2015).
41. Qian, J. & Tang, B.Z. AIE luminogens for bioimaging and theranostics: from organelles to animals. *Chem* **3**, 56-91 (2017).
42. Feng, G. & Liu, B. Aggregation-induced emission (AIE) dots: Emerging theranostic nanolights. *Acc. Chem. Res.* **51**, 1404-1414 (2018).
43. Qin, W.*, et al.* Biocompatible nanoparticles with aggregation-induced emission characteristics as far-red/near-infrared fluorescent bioprobes for in vitro and in vivo imaging applications. *Adv. Funct. Mater.* **22**, 771-779 (2012).
44. Zhao, Z.*, et al.* Highly efficient photothermal nanoagent achieved by harvesting energy via excited-state intramolecular motion within nanoparticles. *Nat. Commun.* **10**, 768 (2019).
45. Wang, D.*, et al.* Boosting non-radiative decay to do useful work: development of multi-modality theranostic system from AIEgen. *Angew. Chem., Int. Ed.* (2019).
46. Liu, S.*, et al.* Moleculer motion in aggregates: manipulating TICT for boosting photothermal theranostics. *J. Am. Chem. Soc.* (2019).

47. Dong, Y.*, et al.* Aggregation-induced and crystallization-enhanced emissions of 1, 2-diphenyl-3, 4-bis (diphenylmethylene)-1-cyclobutene. *Chem. Commun.*, 3255-3257 (2007).
48. Dong, Y.*, et al.* Switching the light emission of (4-biphenylyl) phenyldibenzofulvene by morphological modulation: crystallization-induced emission enhancement. *Chem. Commun.*, 40-42 (2007).
49. Galer, P., Korošec, R.C., Vidmar, M. & Šket, B. Crystal structures and emission properties of the BF2 complex 1-phenyl-3-(3, 5-dimethoxyphenyl)-propane-1, 3-dione: multiple chromisms, aggregation-or crystallization-induced emission, and the self-assembly effect. *J. Am. Chem. Soc.* **136**, 7383-7394 (2014).
50. Yoshii, R., Hirose, A., Tanaka, K. & Chujo, Y. Functionalization of boron diiminates with unique optical properties: multicolor tuning of crystallization-induced emission and introduction into the main chain of conjugated polymers. *J. Am. Chem. Soc.* **136**, 18131-18139 (2014).
51. Cariati, E.*, et al.* Efficient crystallization induced emissive materials based on a simple push–pull molecular structure. *Phys. Chem. Chem. Phys.* **13**, 18005-18014 (2011).
52. Zheng, C.*, et al.* Fluorescence visualization of crystal formation and transformation processes of organic luminogens with crystallization-induced emission characteristics. *Mater. Chem. Front.* **2**, 180-188 (2018).
53. Cao, Y.*, et al.* Aggregation-induced and crystallization-enhanced emissions with time-dependence of a new Schiff-base family based on benzimidazole. *J. Mater. Chem. C* **2**, 3686-3694 (2014).
54. Sun, H.*, et al.* A novel ultrasound-sensitive mechanofluorochromic AIE-compound with remarkable blue-shifting and enhanced emission. *J. Mater. Chem. C* **2**, 5812-5817 (2014).
55. Yang, C.*, et al.* Crystallization-induced red emission of a facilely synthesized biodegradable indigo derivative. *Chem. Commun.* **51**, 3375-3378 (2015).
56. Fateminia, S.A.*, et al.* Nanocrystallization: a unique approach to yield bright organic nanocrystals for biological applications. *Adv. Mater.* **29**, 1604100 (2017).
57. Zhang, X., Bloch, S., Akers, W. & Achilefu, S. Near-infrared molecular probes for in vivo imaging. *Curr. Protoc. Cytom.* **60**, 12.27. 11-12.27. 20 (2012).
58. Niu, G.*, et al.* Specific Two-Photon Imaging of Live Cellular and Deep-Tissue Lipid Droplets by Lipophilic AIEgens at Ultralow Concentration. *Chem. Mater.* **30**, 4778-4787 (2018).
59. Niu, G.*, et al.* Highly photostable two-photon NIR AIEgens with tunable organelle specificity

and deep tissue penetration. *Biomaterials* **208**, 72-82 (2019).

60. Zheng, Z.*, et al.* Bright near-infrared aggregation-induced emission luminogens with strong two-photon absorption, excellent organelle specificity, and efficient photodynamic therapy potential. *ACS Nano* **12**, 8145-8159 (2018).

61. Situ, B.*, et al.* A two-photon AIEgen for simultaneous dual-color imaging of atherosclerotic plaques. *Mater. Horiz.* **6**, 546-553 (2019).

62. Jiang, M.*, et al.* Two-photon AIE bio-probe with large Stokes shift for specific imaging of lipid droplets. *Chem. Sci.* **8**, 5440-5446 (2017).

63. Ding, D.*, et al.* Ultrabright organic dots with aggregation-induced emission characteristics for real-time two-photon intravital vasculature imaging. *Adv. Mater.* **25**, 6083-6088 (2013).

64. Gu, B.*, et al.* Precise two-photon photodynamic therapy using an efficient photosensitizer with aggregation-induced emission characteristics. *Adv. Mater.* **29**, 1701076 (2017).

65. Zhen, S.*, et al.* Efficient red/near-infrared fluorophores based on benzo [1, 2-b: 4, 5-b′] dithiophene 1, 1, 5, 5-tetraoxide for targeted photodynamic therapy and in vivo two-photon fluorescence bioimaging. *Adv. Funct. Mater.* **28**, 1706945 (2018).

66. Qi, J.*, et al.* Aggregation-induced emission luminogen with near-infrared-II excitation and near-infrared-I emission for ultradeep intravital two-photon microscopy. *ACS Nano* **12**, 7936-7945 (2018).

67. Zong, L.*, et al.* Tunable aggregation-induced emission nanoparticles by varying isolation groups in perylene diimide derivatives and application in three-photon fluorescence bioimaging. *ACS Nano* **12**, 9532-9540 (2018).

68. Zhu, Z.*, et al.* Stable and size-tunable aggregation-induced emission nanoparticles encapsulated with nanographene oxide and applications in three-photon fluorescence bioimaging. *ACS Nano* **10**, 588-597 (2015).

69. Mandal, A.K.*, et al.* Three-photon-excited luminescence from unsymmetrical cyanostilbene aggregates: morphology tuning and targeted bioimaging. *ACS Nano* **9**, 4796-4805 (2015).

70. Wang, Y.*, et al.* Aggregation-induced emission luminogen with deep-red emission for through-skull three-photon fluorescence imaging of mouse. *ACS Nano* **11**, 10452-10461 (2017).

71. Müller, M., Squier, J., Wilson, K. & Brakenhoff, G. 3D microscopy of transparent objects using third-harmonic generation. *J. Microsc.* **191**, 266-274 (1998).

72. Tsang, T.Y. Optical third-harmonic generation at interfaces. *Phys. Rev. A* **52**, 4116 (1995).

73. Barad, Y., Eisenberg, H., Horowitz, M. & Silberberg, Y. Nonlinear scanning laser microscopy by third harmonic generation. *Appl. Phys. Lett.* **70**, 922-924 (1997).

74. Squier, J.A., Müller, M., Brakenhoff, G. & Wilson, K.R. Third harmonic generation microscopy. *Opt. Express* **3**, 315-324 (1998).

75. Witte, S.*, et al.* Label-free live brain imaging and targeted patching with third-harmonic generation microscopy. *Proc. Natl. Acad. Sci. USA.* **108**, 5970-5975 (2011).

76. Sasagawa, K. & Tsuchiya, M. Highly efficient third harmonic generation in a periodically poled MgO: LiNbO3 disk resonator. *Appl. Phys. Express* **2**, 122401 (2009).

77. Chang, C.-F.*, et al.* Cell tracking and detection of molecular expression in live cells using lipid-enclosed CdSe quantum dots as contrast agents for epi-third harmonic generation microscopy. *Opt. Express* **16**, 9534-9548 (2008).

78. Lippitz, M., van Dijk, M.A. & Orrit, M. Third-harmonic generation from single gold nanoparticles. *Nano Lett.* **5**, 799-802 (2005).

79. Schwartz, O. & Oron, D. Background-free third harmonic imaging of gold nanorods. *Nano Lett.* **9**, 4093-4097 (2009).

80. Aouani, H., Rahmani, M., Navarro-Cía, M. & Maier, S.A. Third-harmonic-upconversion enhancement from a single semiconductor nanoparticle coupled to a plasmonic antenna. *Nat. Nanotechnol.* **9**, 290 (2014).

81. Shcherbakov, M.R.*, et al.* Enhanced third-harmonic generation in silicon nanoparticles driven by magnetic response. *Nano Lett.* **14**, 6488-6492 (2014).

82. Liu, M.*, et al.* Efficient third harmonic generation in a metal–organic framework. *Chem. Mater.* **28**, 3385-3390 (2016).

83. Abdelwahab, I.*, et al.* Highly enhanced third-harmonic generation in 2D perovskites at excitonic resonances. *ACS Nano* **12**, 644-650 (2017).

84. Cui, L.*, et al.* Organized aggregation of porphyrins in lipid bilayers for third harmonic generation microscopy. *Angew. Chem., Int. Ed.* **54**, 13928-13932 (2015).

85. Xu, Z.*, et al.* Water-miscible organic J-aggregate nanoparticles as efficient two-photon fluorescent nano-probes for bio-imaging. *J. Mater. Chem.* **22**, 17737-17743 (2012).

86. Li, Y.*, et al.* Highly efficient organic photosensitizer with aggregation-induced emission for imaging-guided photodynamic ablation of cancer cells. *Tetrahedron Lett.* (2018).

87. Sun, W.*, et al.* A two-photon fluorescent probe with near-infrared emission for hydrogen

sulfide imaging in biosystems. *Chem. Commun.* **49**, 3890-3892 (2013).

Acknowledgements

This work was supported by the National Science Foundation of China (21788102, 21674040 and 61735016), the Research Grants Council of Hong Kong (16308016, C6009-17G and A-HKUST605/16), the University Grants Committee of Hong Kong (AoE/P-03/08), the Innovation and Technology Commission (ITC-CNERC14SC01 and ITCPD/17-9), the National Key Research and Development program of China (2018YFE0190200), the Science and Technology Plan of Shenzhen (JCYJ20160229205601482), the Zhejiang Provincial Natural Science Foundation of China (LR17F050001) and the Natural Science Foundation for Distinguished Young Scholars of Guangdong Province (2016A030306013).

Author contributions

J.Q. and B.Z.T. conceived and designed the study. Z.Z. synthesized and characterized the compounds. D.L. and J.Q. performed the nonlinear optical property measurements and *in vivo* nonlinear optical imaging experiments. H.H.Y.S. and I.D.W. did the crystal analysis. Z.Z., D.L., Z.L., H.Q.P., R.T.K.K., J.W.Y.L., J.Q. and B.Z.T. analyzed the data and participated in the discussion. Z.Z., D.L., J.Q. and B.T. wrote the manuscript with comments from all authors.

Additional information

Supplementary information is available in the online version of the paper. Reprints and permissions information is available online at www.nature.com/reprints. Correspondence and requests for materials should be addressed to B.Z.T.

Competing interests

The authors declare no competing interests.